Dalton Transactions

ROYAL SOCIETY OF CHEMISTRY

PAPER

View Article Online
View Journal | View Issue

Open Access Article. Published on 30 2024. Downloaded on 20/10/2024 23:30:48.
This article is licensed under a Creative Commons Attribution 3.0 Unported Licence.

Check for updates

Cite this: *Dalton Trans.*, 2024, **53**, 8764

Unlocking room-temperature bistable spin transition at the nanoscale: the synthesis of core@shell $[Fe(NH_2trz)_3(NO_3)_2]@SiO_2$ nanoparticles†

A. Regueiro,[a] M. Martí-Carrascosa,[a,b] R. Torres-Cavanillas *[a,c] and E. Coronado *[c]

Received 27th March 2024,
Accepted 29th April 2024

DOI: 10.1039/d4dt00911h

rsc.li/dalton

In this work, we address the synthesis of stable spin-crossover nanoparticles capable of undergoing a hysteretic spin transition at room temperature. For this purpose, we use the reverse-micelle protocol to prepare naked $[Fe(NH_2trz)_3](NO_3)_2$ and core@shell $[Fe(NH_2trz)_3](NO_3)_2@SiO_2$ nanoparticles. Through meticulous adjustment of synthetic parameters, we achieved nanoparticle sizes ranging from approximately 40 nm to 60 nm. Our findings highlight that $[Fe(NH_2trz)_3](NO_3)_2$ presents a modest thermal hysteresis of 7 K, which decreases by downsizing. Conversely, silica-coated nanoparticles with sizes of *ca.* 60 and 40 nm demonstrate a remarkable hysteretic response of approximately 30 K, switching their spin state around room temperature. Moreover, the presence of a SiO_2 shell substantially enhances the nanoparticles' stability against oxidation. In this context, the larger 60 nm $[Fe(NH_2trz)_3](NO_3)_2@SiO_2$ hybrid remains stable in water for up to two hours, enabling the observation of an unreported water-induced spin transition after 30 min. Therefore, this work also introduces an intriguing avenue for inducing spin transitions through solvent exchange, underscoring the versatility and potential of these nanoparticles.

1. Introduction

Fe^{II}-based spin-crossover (SCO) complexes exhibit great potential as versatile switches in molecular nanodevices, owing to their capability to undergo reversible transitions between high-spin (HS) and low-spin (LS) electronic states in response to various stimuli.[1–4] In this context, synthesizing them as nanoparticles (NPs) makes SCO compounds easier to process and compatible with current nanotechnologies. Furthermore, recent breakthroughs have highlighted the potential of combining SCO nano-objects with two-dimensional materials or metallic nanoparticles (NPs) in order to obtain robust electronic nanodevices for information storage.[5–9]

Nevertheless, prior to their practical implementation, there are significant challenges to overcome. One of the primary hurdles involves synthesizing SCO nanostructures capable of operating under ambient conditions. This is quite challenging, as (1) SCO compounds with spin transitions at room temperature are scarce, and bistability is usually compromised upon miniaturization;[10–13] (2) these types of Fe^{II} compounds are quite unstable against oxidation, due to the tendency of Fe^{II} to oxidize into Fe^{III}, losing the SCO behaviour.[14] This is even more dramatic in aqueous solutions, hampering their use in biomedicine or chemical post-functionalization in aqueous media.[15,16] Therefore, it is imperative to further explore the synthesis of robust SCO compounds to develop bistable SCO nanoparticles with spin transitions occurring at room temperature, kinetically stable HS states, and high resistance to oxidation. In this regard, one of the most interesting approaches relies on the surface protection of the NPs with capping agents,[17] inorganic shells,[18,19] or by confinement inside the cavities of porous materials.[20–22]

Herein, we report the preparation of SCO NPs with a cooperative spin transition at room temperature, along with high stability against oxidation. To do so, we focused on the SCO compound $[Fe(NH_2trz)_3](NO_3)_2$, and synthesized both naked and silica-wrapped nanoparticles of 60 and 40 nm using the reverse-micelle procedure. We selected this SCO compound because it is reported that in bulk it exhibits a cooperative spin transition around room temperature.[25] However, its miniaturi-

[a]Instituto de Ciencia Molecular, Universitat de València, Catedrático José Beltrán 2, 46980 Paterna, Spain. E-mail: ramon.torrescavanillas@materials.ox.ac.uk
[b]Universitat Politecnica de Valencia, Nanophotonics Technology Center, Valencia, Spain
[c]Department of Materials, Oxford University, 21 Banbury Rd, Oxford OX2 6NN, UK. E-mail: Eugenio.coronado@uv.es

† Electronic supplementary information (ESI) available: Details of the characterization of the different compounds described here. See DOI: https://doi.org/10.1039/d4dt00911h

This journal is © The Royal Society of Chemistry 2024

Open Access Article. Published on 30 2024. Downloaded on 20/10/2024 23:30:48.
This article is licensed under a Creative Commons Attribution 3.0 Unported Licence.

zation has been relatively unexplored due to the synthetic challenges involved, particularly the need to synthesize $Fe^{II}(NO_3)_2$ *in situ*. We incorporate an ultrathin silica shell to protect the SCO core against oxidation,[23] and at the same time to enhance the cooperativity between Fe centers.[24] After comparing both systems, we found that the naked NPs have a slightly smaller thermal hysteresis compared to the bulk. In contrast, the core–shell NPs exhibit a larger hysteresis than the bulk around room temperature and are notably more stable in water, remaining unoxidized for up to 2 hours.

2. Experimental section

2.1. Synthetic protocols

All chemical reagents, tetraethyl orthosilicate 98% (Sigma-Aldrich), Triton X-100 (Sigma-Aldrich), ascorbic acid (Sigma-Aldrich), 4-amino-4*H*-1,2,4-triazole (Sigma-Aldrich), iron tetrafluoroborate hexahydrate (Sigma-Aldrich), barium nitrate (Sigma-Aldrich), Silicon Elastomer Sylgard 18 kit (Sigma-Aldrich), polymethyl methacrylate M_w 35 000 (Sigma-Aldrich), *n*-hexanol (Sigma-Aldrich), cyclohexane (Sigma-Aldrich), ultrapure water (18.2 MΩ), ethanol absolute extra dry 99.5% (AcroSeal™) and acetone HPLC grade (Scharlau), were purchased and used without further purification.

SCO-bulk. $Ba(NO_3)_2$ (1.5 mL, 0.7 M) was stirred in a water bath (80 °C) until completely dissolved in water and then mixed with an aqueous solution of $Fe(SO_4)$ (0.5 mL, 1 M). After a few minutes, solid $BaSO_4$ was precipitated, which was separated from the supernatant through filtration, while the Fe $(NO_3)_2$ precursor remained dissolved. The resulting solution was added to an ethanolic solution of 4-amino-4*H*-1,2,4-triazole ligand (1 mL, 3 M). After leaving overnight, the precipitated particles were washed several times with EtOH and finally air-dried for 12 h.

SCO. $Fe(NO_3)_2$ was synthesized using the same protocol reducing the concentration of $Ba(NO_3)_2$ to 0.5 M (0.3 M) and $Fe(SO_4)$ to 0.75 M (0.5 M) for SCO-1 (2). Then 0.5 mL of the filtered solution was added to a freshly prepared organic mixture containing Triton X-100 (1.8 mL), *n*-hexanol (1.8 mL), and cyclohexane (7.5 mL). Then, an aqueous solution of 4-amino-4*H*-1,2,4-triazole ligand (0.5 mL, 4.5 M) was added to a similarly prepared organic solution. Both mixtures were stirred at room temperature for 15 min to produce a stable microemulsion. Finally, both microemulsions were combined and stirred to enable micellar exchange (12 h). NPs were obtained by precipitation upon the addition of acetone (≈30 mL) and collected by centrifugation (9000 rpm, 15 min), followed by 3 cycles of washing with ethanol to remove the excess surfactant. Finally, the powdered sample was air-dried for 24 h.

SCO@SiO$_2$. SCO@SiO_2-1 and 2 were prepared following the same synthetic procedure as used for SCO-1 and 2 upon the addition of tetraethyl orthosilicate (TEOS) (0.1 mL) to both aqueous phases before mixing both microemulsions.

$[Fe(NH_2trz)_{3x}((Htrz)_2(trz))_{1-x}](BF_4)_{1+x}$, and $[Fe(NH_2trz)_{3x}((Htrz)_2(trz))_{1-x}](ClO_4)_{1+x}$ were synthesised following a previously reported protocol.[1b] Their NH_2trz and Htrz ratios were estimated from the initial moles of precursors.

2.2. Physical characterization

NP size distributions in solution were determined in ethanolic 0.1 mg mL^{-1} suspensions by DLS using a Zetasizer ZS instrument (Malvern Instruments, UK). Scanning electron microscopy and energy dispersive spectroscopy studies were carried out on a Hitachi S4800 microscope and, in scanning TEM mode (STEM), using an Oxford Instruments X-MaxN 100TLE detector. Transmission electron microscopy studies were carried out using a Technai G2 F20 microscope operating at 200 kV and a JEM-1010 operating at 100 kV. Samples were prepared by dropping suspensions on lacey formvar/carbon copper grids (300 mesh). The real size distribution was determined by "manual counting" of TEM images using ImageJ software. Attenuated total reflectance Fourier-transform infrared spectra were collected using an ALPHA II FTIR spectrometer (Bruker) in the 4000–400 cm^{-1} range without KBr pellets. Powder-X-ray diffraction measurements were carried out on a PANalytical Empyrean diffractometer using Cu Kα radiation (Cu Kα = 1.5418 Å) with a PIXcel detector, operating at 40 mA and 45 kV. Profiles were collected in the $2° < 2\theta < 45°$ range with a step size of 0.013°. Thermogravimetric analyses were carried out using a Mettler Toledo TGA/SDTA 851e model operating in the 25–700 °C range in air. UV-vis absorption spectra were recorded on a Jasco V-670 spectrophotometer in baseline mode in the 400 to 800 nm range, using Thermo Scientific™ 96-well UV microplate containers. Magnetic data were collected with a Quantum Design MPMS XL-5 susceptometer equipped with a SQUID sensor. DC FC magnetization measurements were performed under an applied magnetic field of 100 Oe at 1 K min^{-1} scan rate in the temperature range between 100 and 400 K. The diamagnetic contributions were corrected using Pascal tables, taking into account the molecular formula of the species $Fe(NH_2trz)_3(NO_3)_2$ only, since the contribution of the SiO_2 shell is negligible in all cases because of its reduced thickness. The γ_{HS} was calculated by applying the following formula: $\gamma_{HS} = 100 \times \chi_M T_{200K}/\chi_M T_{400K}$.

3. Results and discussion

3.1. Synthesis

To prepare both the $Fe(NH_2trz)_3(NO_3)_2$ and Fe $(NH_2trz)_3(NO_3)_2$@SiO_2 NPs (hereinafter called SCO and SCO@SiO_2, respectively), we first synthesized the $Fe(NO_3)_2$ precursor, as it is not commercially available. To do so, we mixed an aqueous solution of $FeSO_4$ with $Ba(NO_3)_2$. After a few minutes, a white solid, which corresponds to $BaSO_4$, is formed, and separated from the supernatant, leaving the Fe $(NO_3)_2$ in solution. To obtain bulk $Fe(NH_2trz)_3(NO_3)_2$ as a reference sample, we mixed freshly synthesized $Fe(NO_3)_2$ with the aminotriazole (NH_2-trz) ligand (see the Experimental section), called from now on SCO-bulk. After 1 hour of reaction, we obtained a purple powder. Scanning electron microscopy

Open Access Article. Published on 30 2024. Downloaded on 20/10/2024 23:30:48.
This article is licensed under a Creative Commons Attribution 3.0 Unported Licence.

(SEM) images of the powder reveal large microcrystals measuring 1.4 ± 0.7 μm in length and 0.7 ± 0.4 μm in width (Fig. S1†).

Next, to confine the growth and prepare NPs of Fe$(NH_2trz)_3(NO_3)_2$, we proceeded with the well-known reverse-micelle protocol. This involves mixing two microemulsions: one containing $Fe(NO_3)_2$, with the other containing the aminotriazole ligand. Each microemulsion comprises an organic phase with a non-ionic surfactant (Triton X-100), a co-surfactant (*n*-hexanol), and an organic phase (cyclohexane), along with the aqueous phase containing either the Fe or the ligand. For the synthesis of the SiO_2-coated NPs, the same protocol was followed, but tetraethyl orthosilicate (TEOS) was added to the aqueous phase before mixing both microemulsions. In this instance, TEOS serves as a precursor of the SiO_2, which envelops the SCO core in the NPs. Upon mixing, in all cases, a purple powder was obtained, which was washed by centrifugation and then air-dried overnight.

In order to control the size of the NPs, we adjusted the concentration of initial precursors, as this proved to be the most effective method.[11,23,24] Table 1 summarizes how concentration affects the size of the hybrid NPs, measured by dynamic light scattering (DLS) of the NPs redispersed in ethanol. Notably, lower initial Fe and ligand concentrations result in smaller NPs, enabling the synthesis of NPs with sizes of *ca.* 60 nm (SCO-1 for the naked NPs and SCO@SiO_2-1 for the core@shell) and 40 nm (SCO-2 for the naked NPs and SCO@SiO_2-2 for the core@shell), as shown in Fig. S2.†

Table 1 Size of the NPs synthesized with different Fe : NH_2trz mol ratios

	Fe^{2+}/mmol	NH_2trz/mmol	Width/nm	Length/nm
SCO-bulk	100	300	1400 ± 700	700 ± 400
SCO-1	0.750	2.250	32 ± 6	68 ± 10
SCO-2	0.500	1.500	—	44 ± 7
SCO@SiO_2-1	0.750	2.250	26 ± 6	62 ± 21
SCO@SiO_2-2	0.500	1.500	37 ± 9	43 ± 9

3.2. Characterization of the SCO and SCO@SiO_2

The morphology of the formed NPs was explored in more detail by transmission electron microscopy (TEM). In contrast to DLS, which provides the hydrodynamic diameter values of the NPs, by using TEM imaging it was possible to obtain not only a more precise size distribution but also to extract information on the morphology of NPs. In this regard, as depicted in Fig. 1, NPs SCO-1 and SCO@SiO_2-1 exhibit a rod-like shape with lengths (widths) of 68(32) ± 10(6) nm, and 62(26) ± 21(6) nm, respectively (Fig. S3†). On the other hand, when the NPs were downsized below 50 nm for SCO-2 and SCO@SiO_2-2, a sphere-like morphology with an average diameter of around 40 nm was obtained. This is due to the 1D nature of the Fe-NH_2trz chains, which exhibit a preferential crystalline axis that becomes more pronounced as the size of the particle increases.[26,27]

To establish the presence of Si, Fe, and O in the different samples, energy-dispersive X-ray spectroscopy (EDS) experiments were performed. As can be seen in Fig. S4†, all the SCO@SiO_2 NPs display the O K and Si K edges expected from the silica shell, while these peaks are absent in all the naked SCO NPs. However, the accurate determination of the shell

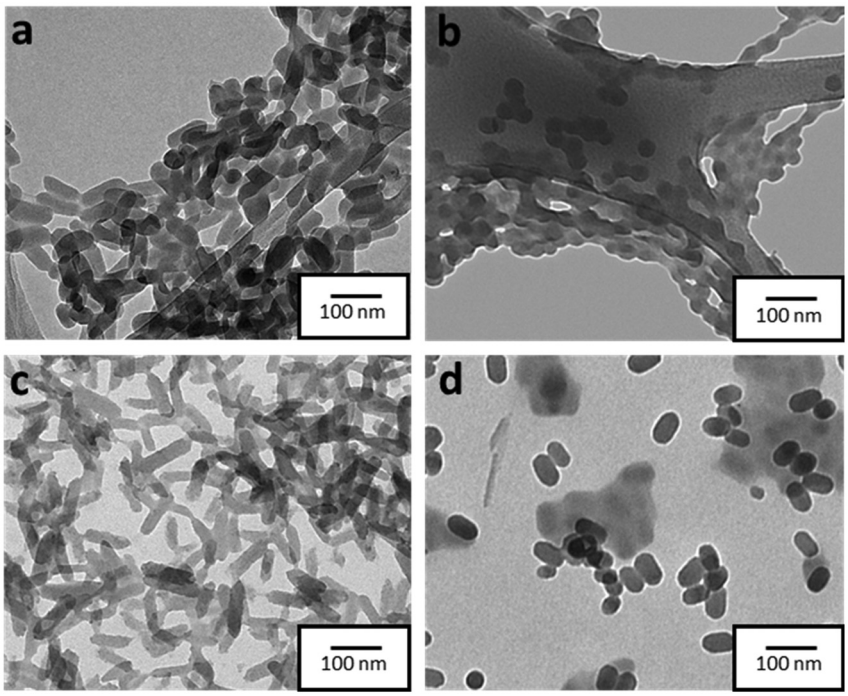

Fig. 1 TEM images of SCO-1 (a), SCO-2 (b), and SCO@SiO_2-1 (c), and 2 (d).

Open Access Article. Published on 30 2024. Downloaded on 20/10/2024 23:30:48.
This article is licensed under a Creative Commons Attribution 3.0 Unported Licence.

thickness proved to be quite challenging due to the reduced SiO_2 shell thickness for such small core@shell NPs. This has already been explored by us, where we observed that our modified reverse-micelle protocol yields a silica shell of less than 1 nm.[23] Later, we proceeded to characterize the structure and composition of both the naked and SiO_2-coated systems by means of attenuated total reflection infrared (ATR-IR) spectroscopy, powder X-ray diffraction (PXRD), thermogravimetric analysis (TGA), and X-ray photoemission spectroscopy (XPS). From the ATR-IR spectra, we could observe in all samples the characteristic vibrational modes of the NH_2trz ligand, including the C=N and N–H stretching modes at around 1600 cm^{-1} and 1500 cm^{-1}, respectively, and a broad band between 3100 and 3300 cm^{-1} from the hydrogen vibration. Finally, the prominent peak of NO_3^- stretching is perfectly visible at approximately 1300 cm^{-1} (Fig. S5†). TGA analysis showed that the miniaturization slightly affects the decomposition temperature, decreasing with the particle size from 214 °C in SCO-bulk to 207 °C in SCO-1, and 205 °C in SCO-2. In contrast, the presence of the silica shell increases the core stability, maintaining the decomposition temperature of the bulk for the SCO@SiO_2-1 (214 °C), and increasing it from 205 °C in SCO-2 to 210 °C for SCO@SiO_2-2 (Fig. S6†). Through XPS, we studied the Fe oxidation state, and further confirmed the presence of the ligand and the NO_3^- anion in the SCO and SCO@SiO_2 samples. All the samples display identical Fe 2p and N 1s regions, as shown in Fig. 2a and b. Regarding the Fe 2p region, the characteristic Fe $2p_{3/2}$ and Fe $2p_{1/2}$ peaks at ~709 and ~722 eV of the Fe^{2+} in the LS (purple band) state, and some extra doublets that are associated with the presence of some oxidized Fe^{3+} or residual Fe^{2+} in the HS (orange, dark yellow and grey bands) state, are present.[28] On the other hand, the N 1s region shows three different bands, one located at ~400 eV coming from the nitrogen atoms in the triazole ring, another at ~402 eV from the NH_2-trz terminal amines, and the last one at ~407 eV that is attributed to the NO_3^- anions (Fig. 2). Finally, the XRD diffractogram of the samples revealed a single phase corresponding to the SCO compound (see Fig. S7†).

Notably, the presence of the silica shell increases not only the thermal stability of $[Fe(NH_2trz)_3](NO_3)_2$ but also its resilience against oxidation. This is evidenced by the fact that the characterization of the NPs was carried out two years after their preparation. Therefore, to further explore their chemical stability in comparison with the naked NPs, we redispersed the SCO-1 and 2, and SCO@SiO_2-1 and 2 NPs in water, which oxidizes bare NPs immediately, and followed the colour change in the suspension by UV-vis. This is possible because, for these compounds, the LS exhibits a prominent absorption band located between 500 and 600 nm, which corresponds to the forbidden Fe^{2+} d–d electronic transition, shifting in the HS state to over 800 nm and lowering its intensity to the point that usually it is not detectable.[29] Notably, when oxidized to Fe^{3+}, this d–d transition shifts to below 400 nm.[30] All this is translated into a colour change from pink for the Fe^{2+} in the LS to white in the HS state, and yellow when oxidized (Fig. S8 and 9†). What we observed is that in the absence of the protective silica shell, the SCO-1 and 2 immediately oxidize, as evidenced by the change in colour from the classical pink of the LS state into yellow, as shown in Fig. S10.† On the other hand, the SCO@SiO_2-1 and 2 are far more stable, holding their stability for around 2 hours prior to their oxidation for the SCO@SiO_2-1, and 1 hour for the smaller SCO@SiO_2-2 (Fig. 2c and S11†). Furthermore, we could observe that after redispersing the SCO@SiO_2-1 in water for 30 min, the NPs switched their spin state from LS to HS, as evidenced by the change to white colour, as shown in Fig. S10–12.† Contrary to the irreversible oxidation that appears after 2 h, the spin transition induced by water is reversible, returning to the initial LS state (pink colour) once the powder is dried in air overnight inside the fume hood (see the ESI, and Fig. S10c†).

This solvent-dependent spin transition is due to the modification of the inter-metallic cooperativity in the SCO compound mediated by the solvent. This effect has already been explored in Fe-trz metal complexes and other coordination polymers.[31,32] Unfortunately, this effect could not be properly observed in the SCO@SiO_2-2, as the compound degraded more

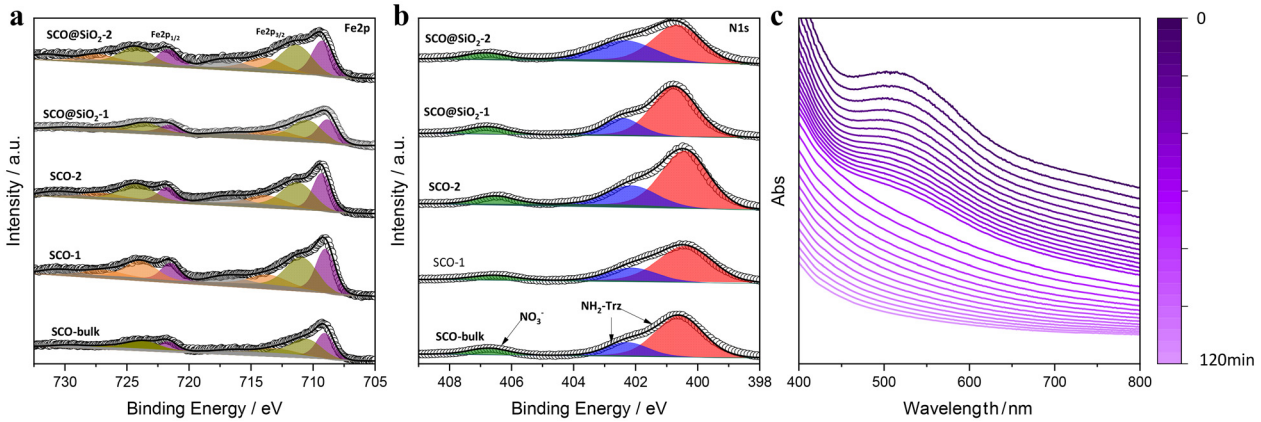

Fig. 2 Spectra from XPS of Fe 2p (a) and N 1s (b) of the different NPs and the bulk. (c) Dependency of the UV-vis absorbance of SCO@SiO_2-1 redispersed in water as a function of time.

Open Access Article. Published on 30 2024. Downloaded on 20/10/2024 23:30:48.
This article is licensed under a Creative Commons Attribution 3.0 Unported Licence.

abruptly than its larger analogue (Fig. S10b†). This can be related to the lower stability associated with the downsizing.

3.3. Study of the spin transition

Once the NPs were properly characterized, we proceeded to study their magnetic properties in detail. As shown in the thermal dependence of χT (Fig. 3 and S13†), all samples displayed a noticeable spin transition within the temperature range of 270 K to 330 K, which is characterized by the hysteresis width (ΔT), and the corresponding transition temperatures $T^{\uparrow}_{1/2}$ (LS to HS) and $T^{\downarrow}_{1/2}$ (HS to LS). However, the magnetic behaviour of the NPs shows significant differences depending on their size. First, size reduction results in a shrinking of the hysteresis width, coupled with a downward shift of the transition temperatures. SCO-bulk (microparticles), 1 (*ca.* 60 nm length), and 2 (*ca.* 40 nm) exhibit progressive reduction in their thermal hysteresis widths from 8 K to 5 K. All the details are summarized in Table 2. These changes stem from the downsizing, which diminishes the cooperativity of the NPs. In addition, we can also observe at low temperatures a χT value higher than the 0 expected for the diamagnetic LS. This is due to the presence of residual HS or oxidized Fe^{3+}, due to the increase of uncompensated Fe at the NP surface as the size of NPs decreases. The silica-coated samples of the SCO@SiO_2-1 (*ca.* 60 nm length) and SCO@SiO_2-2 (*ca.* 40 nm length) exhibit an unprecedented thermal hysteresis for this particular SCO compound. They exhibit a hysteresis width of 30 and 27 K, respectively, and a χT value at 100 K (in the LS state) lower than their uncoated counterparts. From this, we could infer that for the core@shell NPs, the SiO_2 shell is perfectly stabilizing the surface of the NP, protecting it from oxidizing, while constraining its SCO core. The constraint results in the LS to HS transition shifting towards higher temperatures, which is attributed to the pressure exerted by the thin shell. Unlike direct pressure application, which causes a shift in $T^{\uparrow}_{1/2}$ and $T^{\downarrow}_{1/2}$,[33] the pressure from the silica shell increases the hysteresis width rather than simply shifting the transition temperatures.[24] Notably, this effect is more pronounced in this work than in previous works with the SCO $[Fe(Htrz)_2(trz)](BF_4)$ analogue.[19] This can be ascribed to the larger rigidity induced by the deprotonated trz compared to the softer NH_2-trz. This effect can be clearly observed when comparing the thermal hysteresis width of the bulk $[Fe(NH_2trz)_{3x}((Htrz)_2(trz))_{1-x}](BF_4)_{1+x}$ with different ratios of NH_2trz and triazole. The hysteresis decreases as the amount of NH_2trz increases until $3x = 1$, where it stabilizes (ΔT = 6 K), as shown in Fig. S13b.† Furthermore, to dismiss the possibility that this effect is caused by the presence of a different anion, which may play a major role in the compound's cooperativity,[34] we also studied the system $[Fe(NH_2trz)_{3x}((Htrz)_2(trz))_{1-x}](ClO_4)_{1+x}$. As anticipated, this compound exhibited a similar trend to its BF_4^- analogues, showing a decrease in cooperativity with the increase by 3× (Fig. S13c†). Therefore, this demonstrates that the NH_2-trz softening effect is consistently present regardless of the anion.[35] It is important to note that, contrary to the expected increase in the residual high-spin fraction or Fe^{3+} content with downsizing, we observe the opposite effect in SCO@SiO_2-1 and 2 (Table 2). This slight difference can be explained by a higher amount of residual Fe^{3+} in SCO@SiO_2-1 compared to that in SCO@SiO_2-2. We estimated this difference

Table 2 Summary of the magnetic parameters of the different SCO particles

Sample	$T^{\uparrow}_{1/2}$/K	$T^{\downarrow}_{1/2}$/K	ΔT/K	γ_{HS}
SCO-bulk	331	323	8	4
SCO-1	296	289	7	25
SCO-2	310	305	5	18
SCO@SiO_2-1	316	286	30	17
SCO@SiO_2-2	326	299	27	10

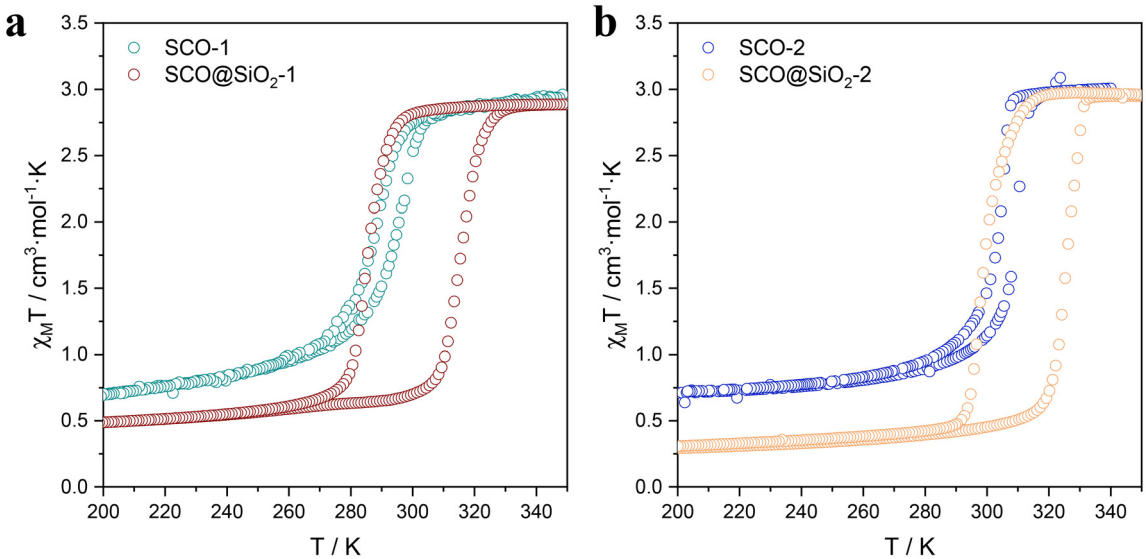

Fig. 3 Comparison of the thermal variation of the $\chi_M T$ product for SCO-1 and SCO@SiO_2-1 (a), and SCO-2 and SCO@SiO_2-2 (b).

 This journal is © The Royal Society of Chemistry 2024

Open Access Article. Published on 30 2024. Downloaded on 20/10/2024 23:30:48.
This article is licensed under a Creative Commons Attribution 3.0 Unported Licence.

to be around 2%, based on the increase in the N 1s NO_3^- signal compared to NH_2-trz. This signal reflects the oxidation state of the Fe centers: the higher the oxidation state, the more NO_3^- is needed to balance the Fe positive charges (Fig. 2). This suggests that, for reasons unrelated to the size of the nanoparticles, a small amount of Fe^{3+} may have been oxidized in the SCO@SiO_2-1, resulting in an increase in the positive charge of the metallo-complex, thus requiring more NO_3^- anions to balance the charges.

Furthermore, as shown in Fig. 3, the SCO@SiO_2 NPs exhibit a spin transition centered right at room temperature for 1 and at 310 K for 2, with a broad hysteresis. Thus, they are ideal systems for devices operating at room temperature. In this context, the last question remaining is for how long the HS can be retained under ambient conditions. To explore this, we studied the retention of the HS of the NPs in an ethanolic suspension of SCO@SiO_2-1 in the HS and the LS states by monitoring the suspension absorption spectra as a function of time. As depicted in Fig. S14,† the absorption spectra of the NPs redispersed in EtOH in the LS state do not vary at all with time. In contrast, the suspension of the HS state NPs exhibits a progressive increase of the 633 nm band typical of the LS state. Still, the HS state is predominant for hours and only recovers completely the pink colour after *ca.* three hours, thus demonstrating the long stability of the HS state under ambient conditions.

4. Conclusions

In conclusion, we have effectively tackled the challenge of synthesizing $[Fe(NH_2trz)_3(NO_3)_2]$ nanoparticles capable of maintaining robust hysteretic spin transitions near room temperature, even for nanoparticles as small as 40 nm, through the strategic coating of NPs with a SiO_2 shell. Our magnetic studies unequivocally demonstrate that SiO_2-coated NPs exhibit a thermal hysteresis width four times larger than that of their uncoated counterparts. This is attributed to the SiO_2 shell constraint, which increases the surface stiffness, and results in a significant broadening of the spin transition hysteresis loop. On the other hand, the presence of the silica shell makes the core far more robust, enabling the NPs to be redispersed in water. Furthermore, thanks to their enhanced stability, we could observe that SCO@SiO_2 NPs of 60 nm experience a reversible water-induced spin transition that has not been explored so far. This breakthrough not only highlights our ability to engineer nanostructures but also opens exciting avenues for tailoring the properties of spin-crossover nanoparticles to suit diverse technological applications.

Author contributions

A. R. and M. C. were responsible for the design, synthesis and characterization of the different materials presented in this work. A.R., and R. T.-C. were in charge of the data interpretation. R.T.-C. designed the work and was involved in the development and coordination of all the experimental parts, discussion of the results and preparation of the manuscript. E.C. supervised all the work and the preparation of the manuscript. All the authors revised and contributed to the presented manuscript.

Conflicts of interest

There are no conflicts to declare.

Acknowledgements

The authors acknowledge the financial support from the European Union (ERC AdG Mol-2D 788222, FET OPEN SINFONIA 964396), the Spanish MCIN (2DHETEROS PID2020-117152RB-100, co-financed by the FEDER, and Excellence Unit "María de Maeztu" CEX2019-000919-M) and the Generalitat Valenciana (PROMETEO Program, PROMETEO/2021/022). This study forms part of the Advanced Materials program and was supported by MCIN with funding from the European Union NextGenerationEU (PRTR-C17.I1) and by the Generalitat Valenciana. R. T.-C. thanks the Generalitat Valenciana for his APOSTD Fellowship (CIAPOS/2021/269), and A. R for his FPI Fellowship (PRE2021-098327). M. M-C. acknowledges funding from the Generalitat Valenciana (Grant No. SEJIGENT/2021/039), the Spanish Ministry of Science and Innovation under project grant PID2021-128442NA-I00 and the European Union ("NextGenerationEU"/PRTR and "ERDF A way of making Europe").

References

1 (*a*) A. Holovchenko, *et al.*, Near Room-Temperature Memory Devices Based on Hybrid Spin-Crossover@SiO_2 Nanoparticles Coupled to Single-Layer Graphene Nanoelectrodes, *Adv. Mater.*, 2016, **28**, 7228; (*b*) J. Krober, E. Codjovi, O. Kahn, F. Groliere and C. Jay, A spin transition system with a thermal hysteresis at room temperature, *J. Am. Chem. Soc.*, 1993, **115**(21), 9810–9811.
2 K. S. Kumar and M. Ruben, Sublimable Spin-Crossover Complexes: From Spin-State Switching to Molecular Devices, *Angew. Chem., Int. Ed.*, 2021, **60**, 7502–7521.
3 J. E. Angulo-Cervera, *et al.*, Thermal hysteresis of stress and strain in spin-crossover@polymer composites: towards a rational design of actuator devices, *Mater. Adv.*, 2022, **3**, 5131–5137.
4 R. Torres-Cavanillas, M. Gavara-Edo and E. Coronado, Bistable Spin-Crossover Nanoparticles for Molecular Electronics, *Adv. Mater.*, 2024, **36**, 2307718.
5 R. Sanchis-Gual, R. Torres-Cavanillas, M. Coronado-Puchau, M. Giménez-Marqués and E. Coronado, Plasmon-assisted spin transition in gold nanostar@spin crossover heterostructures, *J. Mater. Chem. C*, 2021, **9**, 10811–10818.

Open Access Article. Published on 30 2024. Downloaded on 20/10/2024 23:30:48.
This article is licensed under a Creative Commons Attribution 3.0 Unported Licence.

6 R. Torres-Cavanillas, *et al.*, Design of Bistable Gold@Spin-Crossover Core–Shell Nanoparticles Showing Large Electrical Responses for the Spin Switching, *Adv. Mater.*, 2019, **31**, 1900039.
7 R. Torres-Cavanillas, *et al.*, Spin-crossover nanoparticles anchored on MoS_2 layers for heterostructures with tunable strain driven by thermal or light-induced spin switching, *Nat. Chem.*, 2021, **13**, 1101–1109.
8 M. Gavara-Edo, *et al.*, Electrical Sensing of the Thermal and Light-Induced Spin Transition in Robust Contactless Spin-Crossover/Graphene Hybrid Devices, *Adv. Mater.*, 2022, **34**, 2202551.
9 M. Gavara-Edo, *et al.*, Sublimable complexes with spin switching: chemical design, processing as thin films and integration in graphene-based devices, *J. Mater. Chem. C*, 2023, **11**, 8107–8120.
10 L. Salmon and L. Catala, Spin-crossover nanoparticles and nanocomposite materials, *C. R. Chim.*, 2018, **21**, 1230–1269.
11 M. Giménez-Marqués, M. L. García-Sanz De Larrea and E. Coronado, Unravelling the chemical design of spin-crossover nanoparticles based on iron(II)-triazole coordination polymers: Towards a control of the spin transition, *J. Mater. Chem. C*, 2015, **3**, 7946–7953.
12 F. Volatron, *et al.*, Spin-crossover coordination nanoparticles, *Inorg. Chem.*, 2008, **47**, 6584–6586.
13 J. Larionova, *et al.*, Towards the ultimate size limit of the memory effect in spin-crossover solids, *Angew. Chem., Int. Ed.*, 2008, **47**, 8236–8240.
14 L. Trinh, *et al.*, Photoswitchable 11 nm CsCoFe Prussian Blue Analogue Nanocrystals with High Relaxation Temperature, *Inorg. Chem.*, 2020, **59**, 13153–13161.
15 L. Catala and T. Mallah, Nanoparticles of Prussian blue analogs and related coordination polymers: From information storage to biomedical applications, *Coord. Chem. Rev.*, 2017, **346**, 32–61.
16 I. Suleimanov, J. Sánchez Costa, G. Molnár, L. Salmon and A. Bousseksou, The photo-thermal plasmonic effect in spin crossover@silica–gold nanocomposites, *Chem. Commun.*, 2014, **50**, 13015–13018.
17 Y. Raza, *et al.*, Matrix-dependent cooperativity in spin crossover Fe(pyrazine)Pt$(CN)_4$ nanoparticles, *Chem. Commun.*, 2011, **47**, 11501–11503.
18 I. F. Díaz-Ortega, *et al.*, Monitoring spin-crossover phenomena via Re(I) luminescence in hybrid Fe(II) silica coated nanoparticles, *Dalton Trans.*, 2021, **50**, 16176–16184.
19 S. Titos-Padilla, J. M. Herrera, X. W. Chen, J. J. Delgado and E. Colacio, Bifunctional hybrid SiO_2 nanoparticles showing synergy between core spin crossover and shell luminescence properties, *Angew. Chem., Int. Ed.*, 2011, **50**, 3290–3293.
20 G. Zoppellaro, K. Čépe, C. Aparicio, J. Ugolotti and R. Zbořil, Enhancing Magnetic Cooperativity in Fe(II) Triazole-based Spin-crossover Nanoparticles by Pluronic Matrix Confinement, *Chem. – Asian J.*, 2020, **15**, 2637–2641.
21 T. Zhao, *et al.*, Water effect on the spin-transition behavior of Fe(II) 1,2,4-triazole 1D chains embedded in pores of MCM-41, *J. Mater. Chem. C*, 2015, **3**, 7802–7812.
22 T. Zhao, H. Zhu and M. Dong, The nano-confinement effect on the SCO behavior of $[Fe(NH_2trz)_3](NO_3)_2$ 1D chains in MCM-41, *Crystals*, 2020, **10**, 1–8.
23 R. Torres-Cavanillas, *et al.*, Downsizing of robust Fe-triazole@SiO_2 spin-crossover nanoparticles with ultrathin shells, *Dalton Trans.*, 2019, **48**, 15465–15469.
24 (*a*) J. M. Herrera, *et al.*, Studies on bifunctional Fe(II)-triazole spin crossover nanoparticles: Time-dependent luminescence, surface grafting and the effect of a silica shell and hydrostatic pressure on the magnetic properties, *J. Mater. Chem. C*, 2015, **3**, 7819–7829; (*b*) Y. Raza, *et al.*, Matrix-dependent cooperativity in spin crossover Fe(pyrazine)Pt$(CN)_4$ nanoparticles, *Chem. Commun.*, 2011, **47**, 11501–11503.
25 M. M. Dîrtu, *et al.*, Insights into the origin of cooperative effects in the spin transition of $[Fe(NH_2trz)_3](NO_3)_2$: The role of supramolecular interactions evidenced in the crystal structure of $[Cu(NH_2trz)_3](NO_3)_2{\cdot}H_2O$, *Inorg. Chem.*, 2010, **49**, 5723–5736.
26 A. Grosjean, *et al.*, The 1-D polymeric structure of the $[Fe(NH_2trz)_3](NO_3)_2{\cdot}nH_2O$ (with n=2) spin crossover compound proven by single crystal investigations, *Chem. Commun.*, 2011, **47**, 12382–12384.
27 Y. Garcia, *et al.*, Dynamics and supramolecular organization of the 1D spin transition polymeric chain compound $[Fe(NH_2trz)_3](NO_3)_2$. Muon spin relaxation, *J. Phys. Chem. B*, 2007, **111**, 11111–11119.
28 A. Núñez-López, *et al.*, Hybrid Heterostructures of a Spin Crossover Coordination Polymer on MoS_2: Elucidating the Role of the 2D Substrate, *Small*, 2023, **19**, 2304954.
29 (*a*) A. Lapresta-Fernández, *et al.*, Particle tuning and modulation of the magnetic/colour synergy in Fe(ii) spin crossover-polymer nanocomposites in a thermochromic sensor array, *J. Mater. Chem. C*, 2014, **2**, 7292–7303; (*b*) D. Tanaka, N. Aketa, H. Tanaka, T. Tamaki, T. Inose, T. Akai, H. Toyama, O. Sakata, H. Tajiri and T. Ogawa, Thin films of spin-crossover coordination polymers with large thermal hysteresis loops prepared by nanoparticle spin coating, *Chem. Commun.*, 2014, **50**, 10074–10077.
30 V. Vercamer, *et al.*, Diluted Fe^{3+} in silicate glasses: Structural effects of Fe-redox state and matrix composition. An optical absorption and X-band/Q-band EPR study, *J. Non-Cryst. Solids*, 2015, **428**, 138–145.
31 I. Sánchez-Molina, A. Moneo-Corcuera, D. Nieto-Castro, J. Benet-Buchholz and J. R. Galán-Mascarós, Solvent Effect on the Spin State of an Iron(II)-Triazole Trimer, *Eur. J. Inorg. Chem.*, 2021, **2021**, 112–116.
32 D. J. Mondal, S. Roy, J. Yadav, M. Zeller and S. Konar, Solvent-Induced Reversible Spin-Crossover in a 3D Hofmann-Type Coordination Polymer and Unusual Enhancement of the Lattice Cooperativity at the Desolvated State, *Inorg. Chem.*, 2020, **59**, 13024–13028.

 This journal is © The Royal Society of Chemistry 2024

33 (*a*) A. Diaconu, *et al.*, Piezoresistive Effect in the $[Fe(Htrz)_2(trz)](BF_4)$ Spin Crossover Complex, *J. Phys. Chem. Lett.*, 2017, **8**(13), 3147–3151; (*b*) I. Rusu, *et al.*, Pressure gradient effect on spin-crossover materials: Experiment vs theory, *J. Appl. Phys.*, 2021, **129**, 064501.
34 S. Zhao, *et al.*, Anion effects on spin crossover systems: from supramolecular chemistry to magnetism, *Chem. – Eur. J.*, 2023, **29**, e202300554.
35 M. Piedrahita-Bello, *et al.*, Drastic lattice softening in mixed triazole ligand iron(II) spin crossover nanoparticles, *Chem. Commun.*, 2019, **55**, 4769–4772.

Open Access Article. Published on 30 2024. Downloaded on 20/10/2024 23:30:48.
This article is licensed under a Creative Commons Attribution 3.0 Unported Licence.